Title

Imaging striatal dopamine release using a nongenetically encoded near infrared fluorescent catecholamine nanosensor

Journal

Science Advances, 5(7)

ISSN

2375-2548

Authors

Beyene, Abraham G
Delevich, Kristen
Del Bonis-O'Donnell, Jackson Travis
et al.

Publication Date

2019-07-05

DOI

10.1126/sciadv.aaw3108

Peer reviewed

NEUROSCIENCE

Imaging striatal dopamine release using a nongenetically encoded near infrared fluorescent catecholamine nanosensor

Abraham G. Beyene[1], Kristen Delevich[2,3], Jackson Travis Del Bonis-O'Donnell[1], David J. Piekarski[1], Wan Chen Lin[2], A. Wren Thomas[3], Sarah J. Yang[1], Polina Kosillo[4], Darwin Yang[1], George S. Prounis[3], Linda Wilbrecht[2,3]*, Markita P. Landry[1,3,5,6]*

Neuromodulation plays a critical role in brain function in both health and disease, and new tools that capture neuromodulation with high spatial and temporal resolution are needed. Here, we introduce a synthetic catecholamine nanosensor with fluorescent emission in the near infrared range (1000–1300 nm), near infrared catecholamine nanosensor (nIRCat). We demonstrate that nIRCats can be used to measure electrically and optogenetically evoked dopamine release in brain tissue, revealing hotspots with a median size of 2 μm. We also demonstrated that nIRCats are compatible with dopamine pharmacology and show D2 autoreceptor modulation of evoked dopamine release, which varied as a function of initial release magnitude at different hotspots. Together, our data demonstrate that nIRCats and other nanosensors of this class can serve as versatile synthetic optical tools to monitor neuromodulatory neurotransmitter release with high spatial resolution.

INTRODUCTION

The catecholamines dopamine (DA) and norepinephrine (NE) are neuromodulators known to play an important role in learning and attention and are implicated in multiple brain disorders (*1*–*5*). DA, in particular, is thought to play a critical role in learning (*6*), motivation (*7*, *8*), and motor control (*9*), and aberrations in DA neurotransmission are implicated in a wide range of neurological and psychiatric disorders including Parkinson's disease (*10*), schizophrenia (*11*), and addiction (*12*).

Modulatory neurotransmission is thought to occur on a broader spatial scale than classic neurotransmission, the latter of which is largely mediated by synaptic release of the amino acids glutamate (GLU) and γ-aminobutyric acid (GABA) in the central nervous system. In synaptic glutamatergic and GABAergic neurotransmission, neurotransmitter concentrations briefly rise in the synaptic cleft to mediate local communication between the pre- and postsynaptic neurons through the rapid activation of ligand-gated ion channels (*13*). In contrast, neuromodulators (catecholamines and neuropeptides) may diffuse beyond the synaptic cleft and act via extrasynaptically expressed metabotropic receptors (*14*–*19*). Thus, modulatory neurotransmitter activity extends beyond single synaptic partners and enables small numbers of neurons to modulate the activity of broader networks (*20*). The absence of direct change in ionic flux across cell membranes, which is measurable using available tools such as electrophysiology or genetically encoded voltage indicators, has necessitated the use of methods borrowed from analytical chemistry such as microdialysis and amperometry to study the dynamics of neuromodulation. However, the spatial limitations of fast-scan cyclic voltammetry (FSCV) and spatial and temporal limitations of microdialysis narrow our ability to interpret how neuromodulators affect the plasticity or function of individual neurons and synapses.

To understand how neuromodulation sculpts brain activity, we sought to develop new tools that can optically report modulatory neurotransmitter concentrations in the brain extracellular space (ECS) in a manner that is compatible with pharmacology and other available tools to image neural structure and activity. To this end, we designed a synthetic optical probe that can report extracellular catecholamine dynamics with high spatial and temporal fidelity within a unique near infrared (nIR) spectral profile. nIR fluorescent, polymer-functionalized semiconducting single-wall carbon nanotubes (SWNTs) provide a versatile platform for optical probe synthesis to image a diverse set of biomolecular analytes, several of which have shown in vivo functionality (*21*–*23*). In this work, we describe the design, characterization, and implementation of a nanoscale nIR nongenetically encoded fluorescent reporter that allows precise measurement of catecholamine dynamics in brain tissue. This technology makes use of an SWNT noncovalently functionalized with single-strand $(GT)_6$ oligonucleotides to form the nIR catecholamine nanosensor (nIRCat). nIRCats respond to DA with $\Delta F/F$ of up to 24-fold in the fluorescence emission window of 1000 to 1300 nm (*24*), a wavelength range that has shown utility for noninvasive through-skull imaging in mice (*25*).

First, we show in vitro characterization of the nanosensor's specificity for the catecholamines DA and NE and demonstrate its relative insensitivity to the neurotransmitters GABA, GLU, and acetylcholine (ACH), as well as the neuromodulators histamine, serotonin, tyramine, and octopamine. Second, we demonstrate that nIRCats exhibit a fractional change in fluorescence that has the dynamic range and signal-to-noise ratio to report DA efflux in response to brief electrical or optogenetic stimulation of dopaminergic terminals. Next, we use optogenetic stimulation to demonstrate selectivity of the nIRCat nanosensor response to dopaminergic over glutamatergic terminal stimulation. In both stimulation contexts, we show that bath application of D2-type DA receptor antagonist sulpiride and agonist

[1]Department of Chemical and Biomolecular Engineering, University of California, Berkeley, Berkeley, CA, USA. [2]Department of Psychology, University of California, Berkeley, Berkeley, CA, USA. [3]Helen Wills Neuroscience Institute, University of California, Berkeley, Berkeley, CA, USA. [4]Department of Molecular and Cell Biology, University of California, Berkeley, Berkeley, CA, USA. [5]California Institute for Quantitative Biosciences (QB3), Berkeley, CA, USA. [6]Chan Zuckerberg Biohub, San Francisco, CA, USA.
*Corresponding author. Email: landry@berkeley.edu (M.P.L.); wilbrecht@berkeley.edu (L.W.)

quinpirole modulates nIRCat signals in a manner consistent with predicted effects of presynaptic D2 autoreceptor manipulation. These latter experiments can resolve previously undetectable heterogeneity in D2 autoreceptor modulation of presynaptic DA release upon exposure to sulpiride or quinpirole. Last, we show that the presence of a DA reuptake inhibitor yields a prolonged nIRCat fluorescent signal, indicating that the sensors report a change in the time course of DA diffusion and reuptake in striatal brain tissue. These data indicate that nIRCats provide a unique synthetic tool compatible with pharmacology to interrogate the release, diffusion, and reuptake of neuromodulators in neural tissue.

RESULTS

A nIR DA and NE nanosensor

We report nIR fluorescent probes that enable imaging of synaptic and extrasynaptic catecholamines and their release and reuptake dynamics in the ECS of brain tissue. Using a previously established nanosensor generation platform (*26*, *27*), synthetic biomimetic polymers were pinned onto the surface of intrinsically nIR fluorescent SWNTs. The resulting noncovalent nanometer-scale conjugate produced the catecholamine-selective nIRCat (Fig. 1A). In in vitro solution phase experiments (see Materials and Methods), nIRCats exhibited a chirality-dependent maximal change in fluorescence ($\Delta F/F$) of up to 24 (Fig. 1, B and C) with a dynamic range of four orders of magnitude, reporting detectable fluorescence changes from 10 nM to 100 μM DA concentration (fig. S1A). nIRCats were also sensitive to NE with a maximal response of $\Delta F/F = 35$ and a similar dynamic range. We further found that nIRCats had an ~3-fold higher affinity for DA over NE (fig. S1A). nIRCats were insensitive to GABA, GLU, and ACH (Fig. 1C) and could report fluctuations in DA concentration in the presence of ascorbic acid, which is present in cerebrospinal fluid (fig. S1B). nIRCats were also insensitive to octopamine and tyramine, biogenic amines that act as neurotransmitters within invertebrates (Fig. 1C and fig. S1, C and D) and differ from DA by a single hydroxyl group in the case of tyramine or by the placement of a single hydroxyl group in the case of octopamine (fig. S1, C and D). Single-molecule imaging revealed that nIRCat signal in response to repeated perfusions of 10 μM DA was reversible, an important feature for measuring neuromodulator transients (fig. S2). In previous work, we performed stochastic simulations that suggest that nIRCats have sufficient sensitivity to detect physiologically relevant fluctuations in DA concentration in brain tissue arising from the activity of a single dopaminergic terminal, which can briefly exceed concentrations of 1 μM from the release site in a distance-dependent manner (*28*).

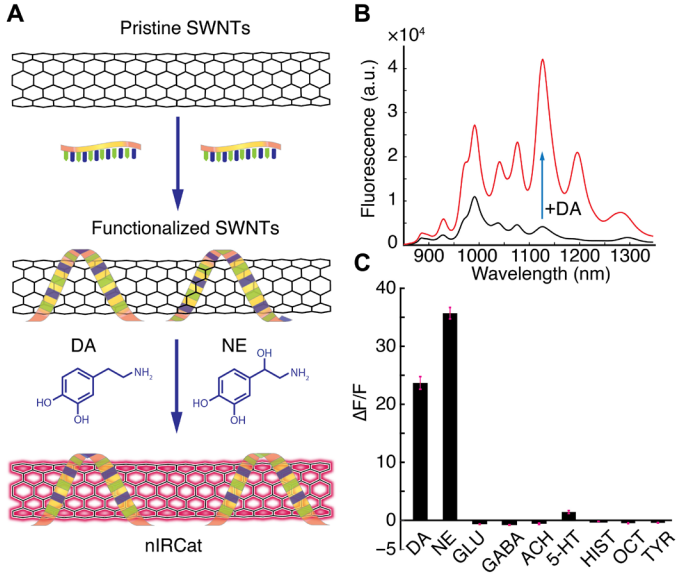

Fig. 1. Synthesis and testing of nIRCats. (**A**) Schematic of optical catecholamine reporters, nIRCats. Pristine SWNTs are functionalized with $(GT)_6$ oligonucleotides to generate turn-on optical reporters for DA and NE. (**B**) Fluorescence spectra of nIRCats before (black) and after (red) the addition of 10 μM of DA in an in vitro preparation in phosphate-buffered saline (PBS; without tissue). Multiple emission peaks correspond to unique SWNT chiralities contained within the multichirality mixture. a.u., arbitrary units. (**C**) Nanosensor optical response to 100 μM DA, NE, GLU, GABA, ACH, serotonin (5-HT), histamine (HIST), octopamine (OCT), and tyramine (TYR) (data from in vitro testing). Black bars represent averages from $n = 3$ independent measurements, and error bars are calculated as SDs of the $n = 3$ measurements.

Imaging of electrical stimulation–evoked DA release in striatal brain tissue

To determine the efficacy of nIRCats for imaging DA in brain tissue, we used brain slices from the dorsal striatum of the mouse. Given that the dorsal striatum is densely innervated by dopaminergic projections from the substantia nigra pars compacta (SNc) but lacks innervation from neurons that release NE (*29*), we leveraged nIRCats capacity to serve as a DA sensor in the striatum. Most of the neurons within the striatum are GABAergic medium spiny neurons (MSNs) with a minority fraction of interneuron populations that include GABAergic and cholinergic interneurons (*30*). Glutamatergic inputs from the cortex and thalamus are the major drivers of MSN activity, and dopaminergic terminals in close proximity to these inputs are thought to play an important role in modulating the activity of MSNs and plasticity at striatal synapses (*31*). Because of the composition of local axons, intrastriatal electrical stimulation is predicted to drive the release of a mix of neurotransmitter, including GABA, GLU, ACH, and DA, but negligible amounts of other catecholamines such as NE.

Coronal mouse brain slices were prepared as described previously (*32*). Slices were subsequently incubated with artificial cerebrospinal fluid (ACSF) containing nIRCats (2 mg/liter) for 15 min to enable sensors to diffuse into the brain tissue (fig. S3A). Slices were subsequently rinsed to remove excess nIRCats and incubated in standard ACSF for another 15 min before imaging. Imaging of nIRCat fluorescence modulation in dorsal striatum was accomplished with a custom-built visible and nIR microscope to enable serial imaging of both visible (400 to 750 nm) and nIR (750 nm to 1700 nm) wavelengths on the same detector (fig. S3B). The nIRCat loading protocol enabled even and widespread labeling of the coronal slices containing the dorsal striatum (fig. S3C). Using this method, Godin *et al.* (*33*) have found that SWNTs localize in ECS. For the imaging procedure, a 785-nm laser for excitation of nIRCats or mercury bulb for generating bright-field images was directed onto the back focal plane of an epifluorescence upright microscope, and imaging channels were selected using a sliding mirror. Serially, either bright-field or nIR images were collected on a Ninox VIS-SWIR 640 broadband camera (Raptor Photonics) with appropriate dichroic filters (see Materials and Methods) and a 60× water-dipping objective (Nikon) providing an

imaging field of 178 μm by 142 μm, likely containing hundreds of dopaminergic terminals.

To investigate striatal neuromodulator release with temporal control of tissue stimulation, we used a bipolar stimulating electrode to evoke terminal release within the dorsomedial striatum of the mouse (stimulus protocol: 3-ms-wide single square pulses over five biological replicates). We found that a single pulse could elicit a nIRCat signal transient (Fig. 2A and movie S1) and that increasing the strength of the stimulus led to larger evoked changes in nIRCat $\Delta F/F$ signal, $(\Delta F/F)_{max}$ [0.1 mA = 0.047 ± 0.025, 0.3 mA = 0.122 ± 0.026, and 0.5 mA = 0.2 ± 0.033 (means ± SD); n = 5 for all measurements; P = 0.008 between 0.1 mA versus 0.3 mA and P = 0.008 between 0.3 mA versus 0.5 mA; Fig. 2B]. Similar responses were additionally obtained in an ex vivo slice of a previously wild-caught species of mouse (*Mus spicilegus*) (fig. S4, A and B). We included *M. spicilegus* to illustrate the potential for nIRCat use in species not typically found in laboratories and in which surgical or genetic manipulation may be a barrier to measurement.

To further test whether evoked nIRCat signals in the mouse tracked striatal DA release and reuptake kinetics, we investigated the effect of nomifensine, a DA reuptake inhibitor that slows the clearance of DA from the ECS by competitively binding to DA transporters (DATs). The addition of 10 μM nomifensine to the bath yielded nIRCat signal with higher peak fluorescence modulation [$(\Delta F/F)_{max}$ = 0.108 ± 0.029 versus 0.189 ± 0.023 (means ± SD); n = 3; P = 0.0178] and a prolonged fluorescent signal compared to signals obtained in ACSF from the same field of view [decay time constant, τ = 2.43 ± 0.24 s versus 10.95 ± 1.15 s (means ± SD); n = 3; P = 0.0002; Fig. 2, A (top versus bottom) and C]. Application of 0 mM extracellular Ca^{2+} ACSF abolished detectable nIRCat responses (P < 0.0001 relative to 2.5 mM Ca^{2+} ACSF), whereas 4 mM Ca^{2+} significantly enhanced evoked $\Delta F/F$ transients (P < 0.0001; Fig. 2D), confirming that nIRCat signals reflect a calcium-dependent process.

To identify nIRCat fluorescence change hotspots (i.e., regions of high $\Delta F/F$), we analyzed our video-rate acquisitions using a custom-built program that accounted for background fluorescence and identified regions with fluctuations in fluorescence intensity in the post-stimulation epoch (see Materials and Methods). We defined nIRCat $\Delta F/F$ hotspots as regions of interest (ROIs) based on a per-pixel stack projection of maximal $\Delta F/F$ in the imaging time series. Using data from single-pulse electrical stimulation experiments, we used custom software that identified ROIs whose sizes varied from 1 to 15 μm, with a log-normal distribution and a median ROI size of 2 μm (Fig. 2, E and F). Repeat stimulations with the same stimulation amplitude in fields of view of the dorsomedial striatum across biological replicates generated similar size distributions (fig. S5A). We found that $\Delta F/F$ hotspots do not necessarily correspond to high nIRCat labeling of the brain tissue, suggesting that the hotspots are a consequence of variation in DA release and not nanosensor loading in the tissue (fig. S5, B to F). Closer examination of several larger ROIs (>5 μm) suggested that these may be composed of smaller hotspots in close proximity (Fig. 2G and fig. S5, B and C).

For further examination of the temporal resolution of nIRCats, we compared the temporal profile of evoked transients measured with nIRCats to transients measured with FSCV. FSCV is a technique that has been widely used to measure temporal catecholamine dynamics both in vivo and in vitro in the striatum and other brain areas (*34*–*36*). FSCV and nIRCat experiments were conducted on separate experimental rigs with the same solutions, temperature settings, electrodes, and stimulation parameters. Evoked transients measured with FSCV (fig. S5G) and nIRCat fluorescence emission showed comparable temporal profiles in the rising phase [latency to peak: FSCV = 0.25 ± 0.0 s versus nIRCat = 0.40 ± 0.18 s (means ± SD); n = 4 fields of view from two biological replicates; P = 0.23]. Meanwhile, nIRCat signals exhibited a wider diversity of decay kinetics [τ: FSCV = 0.51 ± 0.08 s versus nIRCats = 2.43 ± 0.24 s (means ± SD); n = 4 fields of view from two biological replicates; P = 0.0002). A subset of ROIs exhibited decay time constants that overlapped with, or were faster than, those of FSCV signals (Fig. 2, H and I).

We next evaluated the ability of nIRCats to detect DA in the presence of DA receptor drugs. First, using in vitro solution phase experiments (without biological tissue), we found that nIRCat fluorescence intensity was not modulated by exposure to 1 μM concentration of D2 receptor (D2R) antagonists sulpiride and haloperidol, the D2R agonist quinpirole, or the D1R antagonist SCH 23390 (Fig. 3A). Furthermore, with these in vitro solution phase experiments, we showed that DA-induced nIRCat fluorescence signals were not altered in the presence of these same drugs. These data confirmed that nIRCats retained their functionality in the presence of drugs that serve as DA receptor (DAR) agonists and antagonists (Fig. 3A).

We next moved to brain slice where presynaptic DA autoreceptors are known to play a critical role in regulating DA release. In the dorsal striatum of acute slices from n = 3 biological replicates, we found that a D2R agonist suppressed nIRCat transients while a D2R antagonist enhanced them (Fig. 3B). Application of quinpirole (1 μM) suppressed nIRCat fluorescent transients in response to single-pulse electrical stimulation, which recovered following 15-min drug washout (Fig. 3, C and D). Conversely, application of sulpiride (1 μM) significantly increased nIRCat $\Delta F/F$ (Fig. 3, E and F). The effects of these agonists and antagonists were present in ex vivo brain tissue, while they were absent in in vitro solution phase experiments above. Our results are therefore consistent with the powerful inhibition of presynaptic DA release by the D2R agonist quinpirole and the facilitation of presynaptic DA release by the D2R antagonist sulpiride.

Optical recording capability and nanoscale size of nIRCats enables investigation of DA dynamics and pharmacological manipulation with higher spatial resolution than can be achieved using other tools. Therefore, we next examined the effects of quinpirole and sulpiride on individual ROIs (see Materials and Methods). We also used an intermediate dose to provide greater information about differential dose response. We again used electrical stimulation in the dorsal striatum to drive DA release and compared the effect of quinpirole before and after bath application of the drug. We focused on ROIs 4 μm or smaller to capture most of the ROIs while excluding the long tail of larger ROIs that are likely to contain many dopaminergic synapses (Fig. 2, F and G). Averaging all active ROIs 4 μm or smaller, a high (1 μM) concentration of quinpirole yielded post-drug to pre-drug $\Delta F/F$ amplitude ratio of 0.48 ± 0.35 (Fig. 4, A and B). A lower concentration of quinpirole (0.25 μM) resulted in an amplitude ratio of 0.91 ± 0.36 (means ± SD of n = 150 ROIs identified within the field of view; Fig. 4, A and B). We repeated the experiment and analysis with bath application of sulpiride (1 μM) and observed a sulpiride-induced amplitude ratio of 2.34 ± 1.3 (means ± SD of n = 150 ROIs within field of view; Fig. 4, D and E).

Analyses of individual ROIs (all smaller than 4 μm) revealed heterogeneity in ROI responses upon bath application of either quinpirole or sulpiride. Notably, application of quinpirole preferentially suppressed ROIs that exhibited higher $\Delta F/F$ before application of the

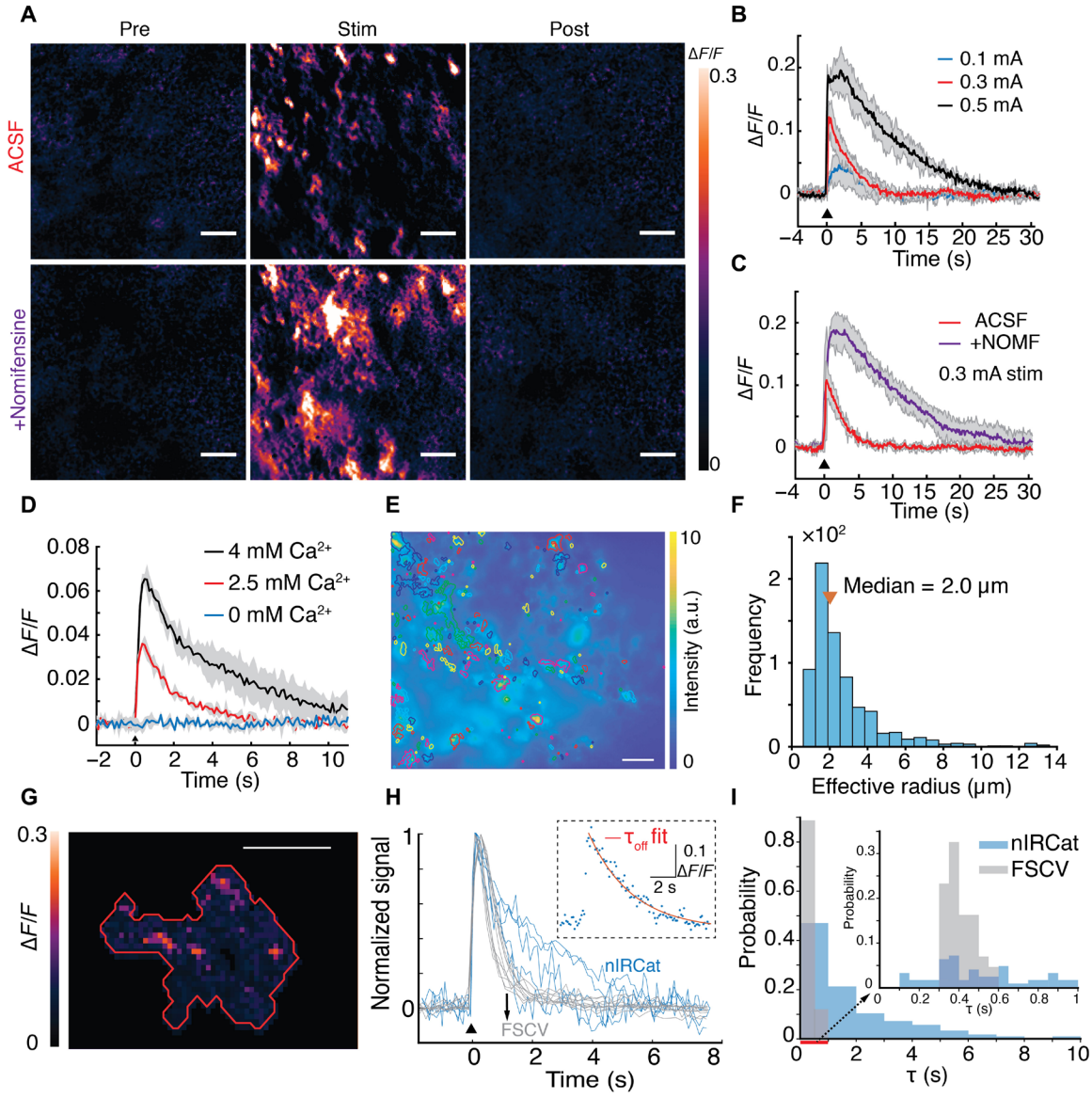

Fig. 2. Imaging and spatiotemporal analysis of DA release evoked by electrical stimulation in striatal tissue. (**A**) Repeat images of the same field of view and Δ*F*/*F* of nIRCat signal after electrical stimulation of 0.3 mA in standard ACSF (top) and in ACSF and 10 μM nomifensine (bottom, +Nomifensine). Three example still frames are presented: "pre" is before electrical stimulation is applied, "stim" represents frame corresponding to peak Δ*F*/*F* following stimulation, and "post" is a frame after nIRCat fluorescence has returned to baseline. Scale bars, 10 μm. (**B**) Nanosensor fluorescence modulation scaled with single-pulse electrical stimulation amplitudes. Field-of-view mean traces and SD bands are presented for three stimulation amplitudes of 0.1, 0.3, and 0.5 mA. (**C**) Time traces of Δ*F*/*F* for 0.3-mA single-pulse electrical stimulation in standard ACSF (red) and in ACSF and 10 μM nomifensine (purple, +NOMF). Mean traces with SD bands are presented. (**D**) nIRCat Δ*F*/*F* responses are abolished in 0 mM Ca^{2+} ACSF and vary with extracellular (Ca^{2+}). (**E**) A single frame from a time series gathered in the dorsomedial striatum showing the entire field of view, overlaid with regions of interest (ROIs) identified using per-pixel Δ*F*/*F* stack projections of nIRCat fluorescence modulation (see Materials and Methods). Color bar represents nIRCat labeling fluorescence intensity. Scale bar, 20 μm. (**F**) Frequency histogram of ROI sizes depicted in (E), exhibiting a log-normal distribution with a median ROI size of 2 μm. (**G**) A higher magnification view of an ROI with an effective radius of 5 μm. Maximum Δ*F*/*F* projection of the ROI shows the presence of smaller fluorescence hotspots within the ROI. Scale bar, 5 μm. (**H**) Overlay of representative normalized FSCV (gray) and nIRCat (blue) traces showing that nIRCat ROI signals exhibit heterogeneity in decay kinetics. Inset: An example of nIRCat experimental data (blue dots) fitted to first-order decay kinetics (red line) to compute decay time constants (τ). (**I**) Normalized frequency histogram of τs computed from FSCV and nIRCat individual ROI time traces. Data from $n = 4$ fields of view representing $n = 2$ biological replicates were pooled. Medians of each distribution: τ = 1.1 s (nIRCats) and τ = 0.4 s (FSCV).

drug [Pearson correlation of $r = -0.21$ ($P = 0.01$) for 0.25 μM data and $r = -0.17$ ($P = 0.03$) for 1 μM data in Fig. 4C]. Additional quinpirole wash-on results are presented in figs. S6 (A to C) and S9. Conversely, our analysis showed that application of sulpiride enhanced nIRCat response in ROIs that had lower Δ*F*/*F* before application of the drug [Pearson correlation of $r = -0.53$ ($P < 0.0001$); Fig. 4F] (see additional data in fig. S6, D and F). Our work uncovers a statistically significant correlation between an ROI's pre-drug Δ*F*/*F* amplitude and its post-drug response. It is possible that the observed heterogeneity in ROI responses maps onto variation in D2 autoreceptor

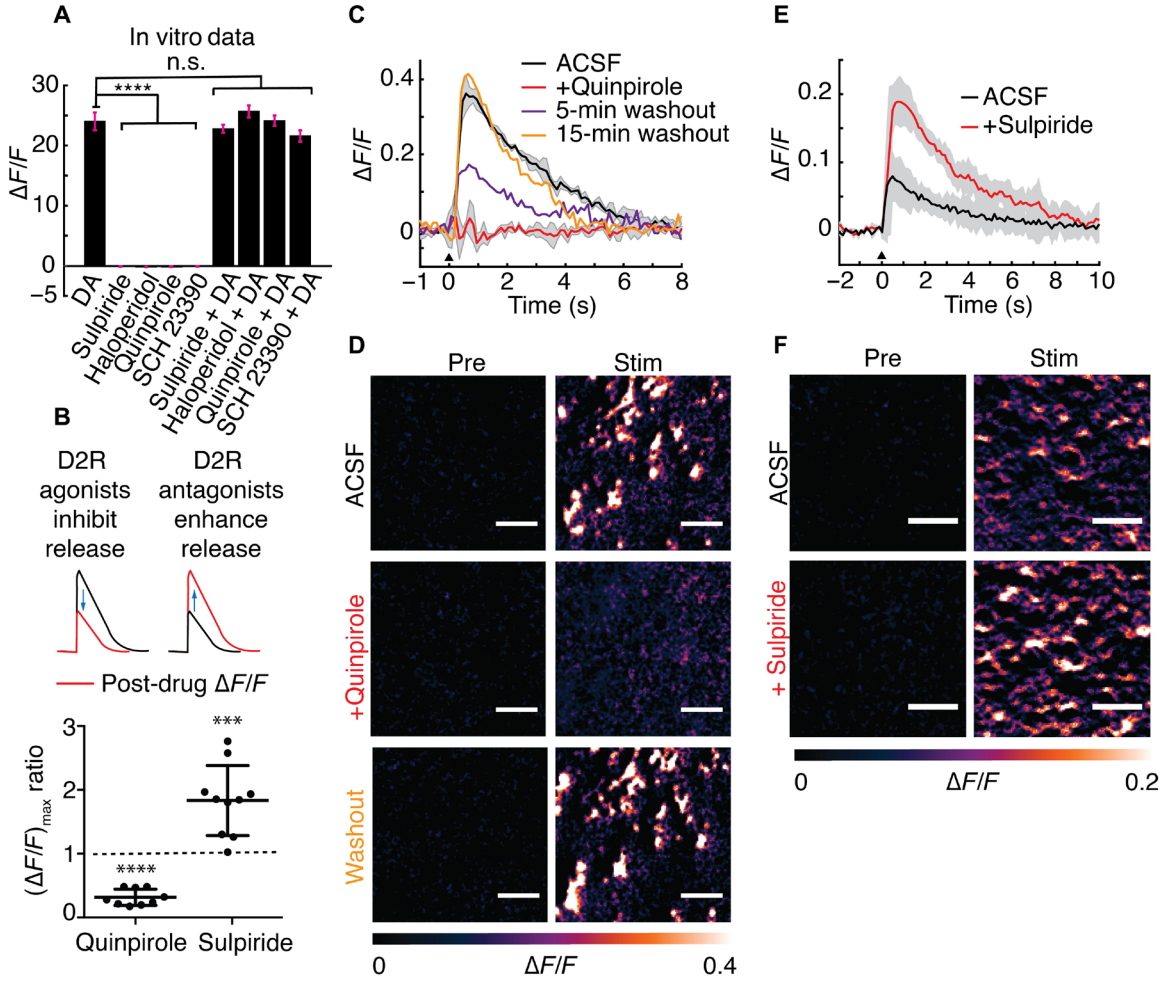

Fig. 3. Imaging DA release in the presence of DA receptor agonists and antagonists. (**A**) In vitro solution phase maximal Δ*F*/*F* (amplitude change at ~1128 nm) of nIRCat in the presence of 100 μM DA; the D2R antagonists sulpiride and haloperidol; D2R agonist quinpirole, and D1R antagonist SCH 23390; and drugs and DA. The addition of 1 μM drug quantities did not induce nIRCat fluorescence modulation in the absence of DA (****$P < 0.0001$ compared to DA Δ*F*/*F*). Subsequent addition of DA to drug-incubated nIRCat solutions produced Δ*F*/*F* responses indistinguishable from DA-only responses. Error bars represent SDs from $n = 3$ measurements. n.s., not significant. (**B**) Top: A schematic of the effect of D2R agonist and antagonist drugs on DA release. Bottom: Quinpirole suppressed nIRCat fluorescence modulation (****$P < 0.0001$), whereas sulpiride facilitated nIRCat fluorescence (***$P = 0.001$) in $n = 3$ biological replicates. Individual data point represents $(\Delta F/F)_{max}$ ratio of the average trace collected in same field of view (post-/pre-drug application). (**C** and **D**) In brain slice, quinpirole (1 μM) suppressed nIRCat fluorescence modulation in response to a single-pulse electrical stimulation (0.5 mA, 3 ms; red trace) compared to pre-drug ACSF (black trace) but recovered following drug washout (purple and orange traces). (**E** and **F**) Sulpiride (1 μM) enhanced nIRCat fluorescence modulation in response to single-pulse electrical stimulation, yielding brighter nIRCat Δ*F*/*F* hotspots compared to drug-free ACSF. Scale bars, 10 μm. All error bands in (C) and (E) represent SD from the mean trace.

expression and/or function (*37*–*40*), but further characterization will be necessary to confirm this hypothesis.

Imaging of optogenetically evoked DA release in striatal tissue

To further confirm that striatal nIRCat nanosensor signals were reporting DA release, we compared channelrhodopsin (ChR2) stimulation of cortical glutamatergic and nigrostriatal dopaminergic terminals in the dorsal striatum. Acute striatal brain slices were prepared from mice virally transfected to express the light-sensitive cation channel ChR2 in either glutamatergic terminals of the striatum [targeted by viral injection in the frontal cortices (ChR2-GLU); Fig. 5A and fig. S7, A and B] or dopaminergic terminals [targeted by viral injection in the midbrain in DAT-Cre mice (ChR2-DA); Fig. 5C and fig. S7C]. Upon optical stimulation of ChR2-DA terminals with a 473-nm laser (five pulses at 25 Hz, 1 mW/mm^2) in the dorsal striatum, we observed significant fluorescence modulation of nIRCat signal (Fig. 5D and movie S2). In contrast, when optogenetic stimulation was targeted at cortical glutamatergic terminals in the striatum, fluorescent nIRCat signals did not rise above baseline fluctuation. Notably, we could confirm in control experiment that optogenetic stimulation of cortical glutamatergic terminals was able to evoke excitatory postsynaptic currents in striatal MSNs (Fig. 5B, inset, and fig. S7, D and E).

Returning to ChR2-DA stimulation, we next varied the number of stimulation pulses (5-ms pulse duration, 25 Hz, 1 mW/mm^2) and observed scaling in nIRCat Δ*F*/*F* amplitude from 1 to 10 pulses ($P = 0.005$) and trend level differences between 1 and 5 pulses ($P = 0.0645$) and between 5 and 10 pulses ($P = 0.086$; Fig. 5E). When we varied the pulse frequency while holding the number of pulses

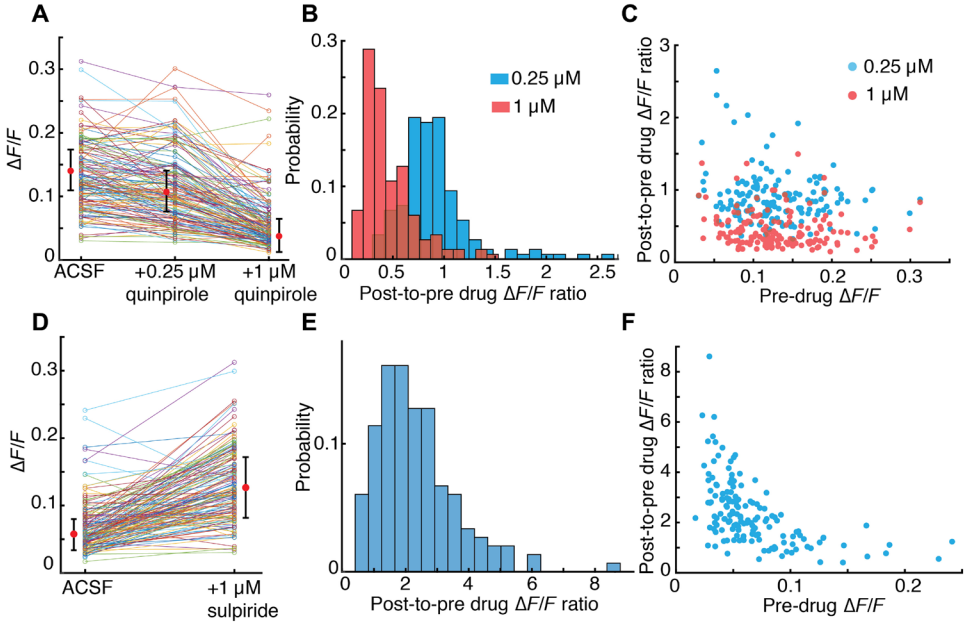

Fig. 4. Effects of quinpirole and sulpiride on nIRCat response at the level of ROIs (4 μm or smaller). (**A**) Δ*F*/*F* of ROIs in ACSF and in ACSF with 0.25 μM and 1 μM of quinpirole. Each Δ*F*/*F* data point corresponding to an ROI is an average from *n* = 3 stimulation repeats. (**B**) Distribution of nIRCat response attenuation upon the addition of 0.25 μM (blue) or 1 μM (red) quinpirole for ROIs in (A). (**C**) Scatter plot of response to drug versus pre-drug Δ*F*/*F* amplitude for data in (A). (**D**) Δ*F*/*F* of ROIs in ACSF and following the addition of 1 μM of sulpiride. Each Δ*F*/*F* data point corresponding to an ROI is an average from *n* = 3 stimulation repeats. (**E**) Distribution of post-to-pre drug Δ*F*/*F* ratio for data in (D). (**F**) Scatter plot of response to drug versus pre-drug Δ*F*/*F* amplitude for data in (D). For (A) and (D), means and error bars (SD) are presented next to each distribution.

constant at five, we observed scaling with significant differences detectable between 1 and 10 Hz ($P = 0.036$). The amplitude difference between 10 and 25 Hz did not reach significance ($P = 0.179$; Fig. 5F). In single-pulse experiments in which we varied pulse width, nIRCat fluorescence responses scaled with pulse duration. This effect was significant when comparing 2 to 5 ms ($P = 0.002$), but the difference from 5 to 10 ms did not reach significance ($P = 0.055$; Fig. 5G).

Last, we tested the effect of dopaminergic pharmacological agents on optogenetically evoked DA release (ChR2-DA). Bath application of quinpirole (1 μM) powerfully suppressed nIRCat fluorescence ($P < 0.0001$), and this effect was reversed after drug washout (Fig. 5H). Consistent with results from electrical stimulation, optogenetic stimulation also showed that quinpirole preferentially suppressed the most active ROIs (fig. S8). Nomifensine (10 μM) enhanced nIRCat signal decay time, consistent with the predicted slowing of DA clearance from the ECS (fig. S9).

DISCUSSION

To understand how neuromodulation alters the plasticity and activity of distinct populations of neurons, there is a need for new optical tools that can measure the extracellular dynamics of neuromodulator release and reuptake at spatiotemporal resolution commensurate with methods used to record neural activity (e.g., electrophysiology and calcium imaging). Here, we demonstrated the feasibility of using a nongenetically encoded fluorescent sensor, nIRCat, to enable optical detection of catecholamine release and reuptake with subsecond temporal and micrometer spatial resolution. We used electrical and optogenetic methods in striatal brain tissue to demonstrate that nIRCat fluorescent signals faithfully report evoked DA release and pharmacologically induced changes in DA dynamics.

We focused nIRCat imaging experiments within the dorsal striatum, a region that receives dense dopaminergic innervation and negligible norepinephrinergic innervation (*29*). Therefore, while nIRCats may not be selective for DA over NE, nIRCats effectively function as a DA sensor within the context of the striatum. Given that striatal DA regulates fundamental processes, including motor function, motivation, and learning, nIRCats represent an important addition to the neuroscience investigative toolkit. Furthermore, of the biogenic amines present in invertebrate species (DA, tyramine, octopamine, serotonin, and histamine), we demonstrated in vitro that nIRCats are exclusively sensitive to DA. Hence, for invertebrate species such as drosophila, we predict that nIRCats may serve as selective and highly sensitive DA sensors throughout the brain.

While other tools are emerging to optically report DA fluctuations via cell surface–engineered proteins (*41*, *42*), nIRCats are likely to fulfill a niche among currently available methods for detecting DA neurotransmission because of their unique nIR fluorescence, the fact that they do not rely on genetic delivery and expression, their relative ease of deployment, and their functionality in the presence of pharmacological DA receptor ligands. This is in contrast to receptor-based fluorescent sensors, which currently cannot report on endogenous DA dynamics in the presence of ligands to the engineered receptor but do exhibit selectivity for DA over NE (*41*, *42*). Furthermore, the synthetic nature of nIRCats eliminates concern about potential G protein–coupled receptor–mediated residual signaling that may be present in protein-based optical probes. nIRCats also offer spatial advantages over FSCV, and our initial experiments suggest that the temporal resolution of the nIRCat signal can be comparable to that of FSCV. nIRCat fluorescence decay profiles exhibit a wider temporal range than that observed from FSCV data and included a significant number of ROIs that showed seconds-long

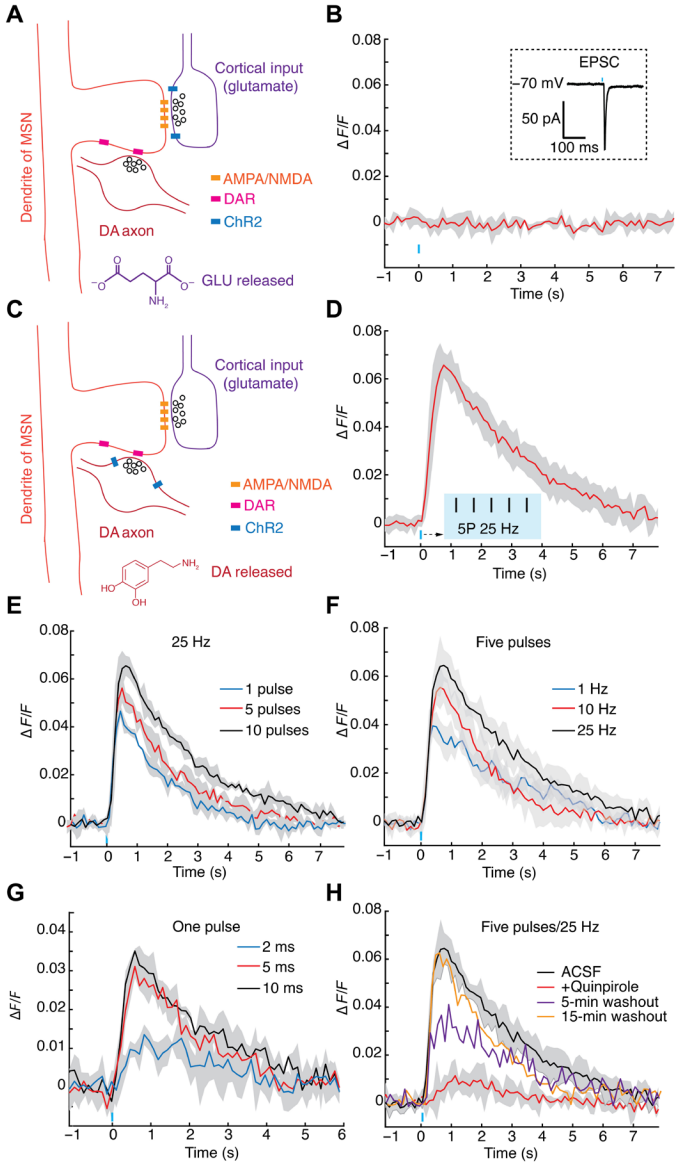

Fig. 5. nIRCat detection of striatal DA release evoked by optogenetic stimulation. (**A**) Schematic of ChR2 expression in cortical glutamatergic terminals synapsing in the dorsal striatum. AMPA, α-amino-3-hydroxyl-5-methyl-4-isoxazolepropionate; NMDA, *N*-methyl-D-aspartate; DAR, DA receptor. (**B**) No nIRCat fluorescence modulation was observed after stimulation of glutamatergic terminals. Inset: GLU release was confirmed by excitatory postsynaptic current (EPSC) on MSN. (**C**) Schematic of ChR2 expression in nigrostriatal dopaminergic terminals of the dorsal striatum. (**D**) Stimulation of dopaminergic terminals resulted in nIRCat fluorescence modulation. Stimulation protocol in (B) and (D) was five pulses (5P) at 25 Hz and a power flux of 1 mW/mm^2, and each pulse had a duration of 5 ms. (**E**) nIRCat Δ*F*/*F* in response to increasing number of pulses delivered at 25 Hz (5-ms pulse duration). (**F**) nIRCat Δ*F*/*F* in response to increasing pulse frequency (1, 10, and 25 Hz) of five pulses. Each pulse had a duration of 5 ms. (**G**) nIRCat Δ*F*/*F* in response to single pulses of 2-, 5-, and 10-ms duration. (**H**) Bath application of 1 μM of quinpirole suppresses DA release and results in depressed nIRCat Δ*F*/*F*. Drug washout rescues DA release and nIRCat Δ*F*/*F*. All error bands represent SD from the mean trace.

time constants in addition to time constants faster than those measured by FSCV. It is debatable whether these results capture the unique spatial properties of specific striatal ROIs or are related to tool differences alone. nIRCats should also sample catecholamine concentration at a smaller spatial scale compared to FSCV. Each distributed nIRCat construct can act as a probe within the ECS and therefore yield a "higher resolution" picture of neuromodulatory dynamics. Future experiments will investigate how the heterogeneity of nIRCat signals (amplitude, kinetics, and modulation by drugs) relates to structural and functional properties at DA terminals and within the ECS. We predict that new optical tools for measuring DA dynamics with high spatial resolution will enable new insights into the regulation of DA release and reuptake at the level of individual synapses (*43*–*45*).

Furthermore, we see potential for future expansion of a larger family of SWNT-based nIR nanosensors (nIRNSs) similar to nIRCats for multiple neurochemical imaging applications. Several lines of evidence illustrate their future potential. First, nIRNSs are easily functionalized with a wide range of synthetic molecular recognition moieties, affording fine control of their surface functional elements and their interactions with the local chemical environment (*22*, *46*, *47*). SWNT fluorescence can be finely tuned to monochromatic emission in the nIR II window (1000 to 1700 nm) by controlling the SWNT chirality (*48*). This chirality-dependent fluorescence in the nIR II window provides further avenues for simultaneously designing color-specific responses to multiple molecular analytes, thereby affording synthesis of ratiometric and multiplexed analyte imaging platforms, as we have shown previously (*49*). Second, SWNT-based nanosensors rely on nIR fluorescence, which greatly reduces the impact of tissue scattering in the emission window and therefore may enable through-cranium imaging (*25*). nIRNSs are compatible with multiphoton imaging with an excitation of 1600 nm (*50*) and, as such, could permit nanoscale imaging of intact neuronal structures pending parallel developments in all-infrared microscopy, as has been shown with visible wavelength-emitting fluorophores (*51*). Third, nIRNSs exhibit robust nonphotobleaching photostability, allowing their use in long-term imaging experiments (*52*). Fourth, because nIRNSs are not genetically encoded, they could enable use in species where gene delivery and protein expression are intractable, time-consuming, or undesirable. Last, the nanosecond-scale binding kinetics and nanoscale dimensions of nIRNSs are likely to enable generation of other neuromodulator nanosensors with improved temporal and spatial resolution. In summary, nIRCats are versatile catecholamine probes amenable to multiplexing with existing tools for concurrent investigation of dopaminergic neuromodulation with other core mechanisms of brain function.

MATERIALS AND METHODS

Nanosensor synthesis

$(GT)_6$ oligonucleotides were purchased from Integrated DNA Technologies (standard desalting). HiPco SWNTs were purchased from NanoIntegris (batch no. HR27-104). $(GT)_6$-SWNT colloidal suspension (nIRCat) was prepared by mixing 1 mg of $(GT)_6$ and 1 mg of SWNTs in 1 ml of a 100 mM NaCl solution. The solution was bath-sonicated (Branson Ultrasonic 1800) and probe tip-sonicated (Cole-Parmer Ultrasonic Processor, 3-mm tip in diameter, 5 W power) for 10 min each in an ice-bath. The sonicated solution was incubated at room temperature for 30 min. The product was subsequently centrifuged at 16,000*g* (Eppendorf 5418) for 90 min to remove unsuspended SWNT bundles and amorphous carbon, and the supernatant was recovered for characterization and use. Each nanosensor suspension was stored at 4°C until use.

Nanosensor characterization

To characterize nIRCats after synthesis, the full visible and nIR absorption spectrum was taken for each nanosensor batch (UV-VIS-nIR spectrophotometer, Shimadzu UV-3600 Plus) or UV-VIS (Thermo Fisher Scientific Genesys 20). SWNT concentrations of as-made nanosensor batches were determined using absorbance at 632 nm (UV-VIS) with an extinction coefficient of $\varepsilon = 0.036$ (mg/liter)$^{-1}$ cm^{-1}. Full spectrum absorbance measurements were made with UV-VIS-nIR after dilution to an SWNT concentration of 5 mg/liter in 100 mM NaCl. For fluorescence spectroscopy, each sensor batch was diluted to a working concentration of 5 mg/liter in 100 mM NaCl, and aliquots of 198 µl were placed in each well of a 96-well plate (Corning). Fluorescence measurements were obtained with a 20× objective on an inverted Zeiss microscope (Axio Observer D1) coupled to a Princeton Instruments spectrograph (SCT 320) and a liquid nitrogen–cooled Princeton Instruments InGaAs linear array detector (PyLoN-IR). A 721-nm laser (Opto Engine LLC) was used as the excitation light source for all characterization experiments.

Neurotransmitter library and dopamine receptor drug screening

For neurotransmitter response screens, we collected the nIR fluorescence spectrum from 198 µl aliquots of nanosensor (an SWNT concentration of 5 mg/liter) before and after the addition of 2 µl of 10 mM solutions of each analyte neurotransmitter (for a 100 µM final analyte concentration in each well of a 96-well plate). All neurotransmitter analytes were purchased from Sigma-Aldrich. Neurotransmitter analytes were incubated for 5 min before taking post-analyte fluorescence measurements. Responses were calculated for the integrated fluorescence count as $\Delta F/F_0 = (F - F_0)/F_0$, where F_0 is the total fluorescence before analyte addition and F is the total fluorescence after analyte addition or for peak fluorescence change corresponding to the (*9*, *4*) SWNT chirality (center wavelength, ~1128 nm). All measurements were made in triplicate. Reported results are means ± SD of the triplicate measurements. All nIRCat nanosensor batches were tested for catecholamine responses before use for tissue catecholamine imaging. DA receptor drugs were purchased from Tocris Bioscience (quinpirole and sulpiride), Abcam (SCH 23390), and Sigma-Aldrich (haloperidol). nIRCat fluorescence modulation to DRDs was measured after the addition of 1 µM drug quantities (final concentration in well) in each well. Post-drug fluorescence spectra were taken after 5-min drug incubation. To measure nIRCat response to DA in the presence of drugs, DA aliquots were added to each drug-incubated well to obtain 100 µM of DA, and post-DA fluorescence spectra were taken after an additional 5-min incubation period.

Nanosensor reversibility testing

A 1.5 glass coverslip was functionalized with 3-aminopropyltriethoxysilane (APTES; Sigma-Aldrich) by soaking in 10% APTES in ethanol for 5 min. The coverslip was then rinsed with deionized water and left to dry. The coverslip was then fixed onto an ibidi sticky-Slide VI 0.4 forming six microfluidic channels. First, 100 µl of phosphate-buffered saline (PBS) was pipetted through a channel. Next, the channel was filled with 50 µl of a solution (5 mg/liter) of nIRCats and left to incubate at room temperature for 5 min. The channel was rinsed using three 50 µl of PBS washes, keeping the channel filled with solution at all times. The surface-immobilized nIRCats in PBS were imaged on an epifluorescence microscope with an excitation of 721 nm and a Ninox VIS-SWIR 640 camera (Raptor). One end of the flow channel was connected to a syringe pump (Harvard Apparatus) using Luer lock fittings. Before the start of image acquisition, the opposite flow reservoir was filled with PBS, and the pump was set to refill mode at a volumetric flow rate of 40 µl min^{-1}. Once the liquid in the reservoir was depleted, 40 µl of 10 µM DA in PBS was added. The process was repeated using alternating additions of 80 µl of PBS washes and 40 µl of DA solution.

Acute slice preparation and nanosensor labeling

Mice were C57BL/6 strain (60 days old), and both male and female mice were used. Mice were group-housed after weaning at postnatal day 21 (P21) and kept with nesting material on a 12:12 light cycle. All animal procedures were approved by the University of California Berkeley Animal Care and Use Committee. Acute brain slices were prepared using established protocols (*32*). Briefly, mice were deeply anesthetized via intraperitoneal injection of ketamine/xylazine cocktail, and transcardial perfusion was performed using ice-cold cutting buffer (119 mM NaCl, 26.2 mM $NaHCO_3$, 2.5 mM KCl, 1 mM NaH_2PO_4, 3.5 mM $MgCl_2$, 10 mM glucose, and 0 mM $CaCl_2$), after which the brain was rapidly extracted. The cerebellum and other connective tissues were trimmed using a razor blade, and the brain was mounted onto the cutting stage of a vibratome (Leica VT1200 S). Coronal slices (thickness, 300 µm) including the dorsal striatum were prepared. Slices were incubated at 37°C for 60 min in oxygen-saturated ACSF (119 mM NaCl, 26.2 mM $NaHCO_3$, 2.5 mM KCl, 1 mM NaH_2PO_4, 1.3 mM $MgCl_2$, 10 mM glucose, and 2 mM $CaCl_2$) before use. Slices were then transferred to room temperature for 30 min before starting imaging experiments and were maintained at room temperature for the remainder of experimentation.

For nanosensor labeling, slices were transferred into a small volume brain slice incubation chamber (Scientific Systems Design Inc., AutoMate Scientific) and kept under oxygen-saturated ACSF (total volume, 5 ml). One hundred microliters of nIRCat nanosensor (100 mg/liter) was added to the 5-ml volume, and the slice was incubated in this solution for 15 min. The slice was subsequently recovered and rinsed in oxygen-saturated ACSF to wash off nIRCats that did not localize into the brain tissue. The rinsing step was performed by transferring the slice through three wells of a 24-well plate (5 s in each well), followed by transfer to the recording chamber with ACSF perfusion for a 15-min equilibration period before starting the imaging experimentation. All imaging experiments were performed at 32°C.

Acute slice preparation for FSCV recording

Acute slices were prepared as described previously. Extracellular DA concentration evoked by local electrical stimulation was monitored with FSCV at carbon fiber microelectrodes (CFMs) using a Millar voltammeter. CFMs were ~7 µm in diameter encased in glass capillary pulled to form a seal with the fiber and cut to final tip length of 70 to 120 µm. The CFM was positioned ~100 µm below the tissue surface at a 45° angle. A triangular waveform was applied to the CFM scanning from −0.7 to +1.3 V and back, against Ag/AgCl reference electrode at a rate of 800 V/s. Evoked DA transients were sampled at 8 Hz, and data were acquired at 50 kHz using AxoScope 10.5 (Molecular Devices). Oxidation currents evoked by electrical stimulation were converted to DA concentration from post-experimental calibrations. Recorded FSCV signals were identified as DA by comparing oxidation (+0.6 V) and reduction (−0.2 V) potential peaks from experimental voltammograms with currents recorded during calibration with 2 µM DA dissolved in ACSF. For stimulation, a

bipolar stimulation electrode (FHC CBAEC75) was positioned on top of the brain slice and approximately 100 μm away from the CFM. Following 30-min slice equilibration in the recording chamber, DA release was evoked using a square pulse (pulse amplitude, 0.3 mA; pulse duration, 3 ms) controlled by an ISO-Flex stimulus isolator (A.M.P.I) and delivered out of phase with the voltammetric scans. Stimulation was repeated three times. To compare FSCV and nIRcat data, each signal was normalized against its peak value [$(DA)_{max}$ or $(\Delta F/F)_{max}$] and coaligned at stimulation time. Latency to peak was computed as $t_{peak} - t_{stim}$, where t_{peak} is the time at which peak signal is attained, and t_{stim} is time of stimulation. Decay time constants (τ) were computed from model fits to a first-order decay process.

Microscope construction and slice imaging

Ex vivo slice imaging was performed with a modified upright epifluorescent microscope (Olympus, Sutter Instruments) mounted onto a motorized stage. Nanosensor excitation was supplied by a 785-nm CW DPSS (continuous-wave diode-pumped solid-state) laser with adjustable output power to a maximum of 300 mW and a near TEM00 top hat beam profile (Opto Engine LLC). The beam was expanded using a Keplerian beam expander composed of two plano-convex lenses (f = 25 and 75 mm; AR coating B, Thorlabs) to a final beam diameter of approximately 1 cm. The beam was passed through a custom fluorescence filter cube [excitation: 800 nm shortpass (FESH0800), dichroic: 900 longpass (DMLP990R), and emission: 900 longpass (FELH0900); Thorlabs] to a 60× Apo objective (numerical aperture, 1.0; working distance, 2.8 mm; water dipping; high nIR transmission; Nikon CFI Apo 60XW nIR). Emission photons collected from the sample were passed through the filter cube, were focused onto a two-dimensional InGaAs array detector [500 to 600 nm: 40% quantum efficiency (QE); 1000 to 1500 nm: >85% QE; Ninox 640, Raptor Photonics], and were recorded using the Micro-Manager Open Source Microscopy Software (*53*). Laser power was adjusted to maximize collected photons and to fill the pixel bit depth on the detector but did not exceed 70 mW at the objective back focal plane. Yellow fluorescent protein (YFP) was imaged by switching the filter cube (U-N41017XL, Olympus) and by using a mercury-vapor lamp (Olympus) for excitation.

Electrical and optical stimulation–evoked DA imaging with nIR microscopy

For electrical stimulation experiments, a bipolar stimulation electrode was positioned in field of view within the dorsomedial striatum identified using a 4× objective (Olympus XLFluor 4×/340). Using 60× objective, the stimulation electrode was brought into contact with top surface of the brain slice and an imaging field of view was chosen at a nominal distance of 150 μm from the stimulation electrode within the dorsomedial striatum. All stimulation experiments were recorded at video frame rates of 9 frames per second (nominal), and single-pulse electrical stimulations were applied after 200 frames of baseline were acquired. Each video acquisition lasted 600 frames. Stimulation amplitudes were staggered, and each stimulation amplitude was repeated three times within a field of view. Slices were allowed to recover for 5 min between each stimulation, with the excitation laser path shuttered. For optogenetic stimulation, a fiber-coupled 473-nm blue laser (Opto Engine LLC DPSS) was positioned in close proximity to the brain slice using a micromanipulator. Expression of ChR2 was confirmed via visible fluorescence imaging, and an imaging field of view was chosen in dorsomedial striatum with robust expression level. Stimulation pulses (five pulses, 5-ms duration per pulse at 25 Hz, 1 mW/mm^2) were delivered after acquiring 200 baseline frames, and the video acquisition lasted 600 frames at nominal 9 frames per second. Drugs were bath-applied to the imaging chamber through ACSF perfusion. ACSF with 10 μM of nomifensine or 1 μM of each drug was used. When the effect of a drug was needed to be evaluated, stimulation/imaging experiments were carried out with drug-free ACSF in an imaging field of view to collect drug-free data. Normal ACSF was then switched to ACSF prepared with the drug of interest and applied for 10 min before stimulation/imaging experiments resumed.

Viral transfection of mice for optogenetic stimulation

Adult male and female mice (>P60) were used for all surgeries. Bilateral viral injections were performed using previously described procedures (*54*) at the following stereotaxic coordinates: 1.94 mm from bregma, 0.34 mm lateral from midline, and 0.70 mm vertical from cortical surface for dorsomedial prefrontal cortex (dmPFC) and −3.08 mm from bregma, 1.25 mm lateral from midline, and 4.0 mm vertical from cortical surface for SNc. For glutamatergic corticostriatal axon stimulation experiments, mice were bilaterally injected with 0.5 μl of CAG-ChR2-EYFP (enhanced YFP) virus into dmPFC. For nigrostriatal dopaminergic axon stimulation experiments, DAT-Cre mice were injected with 0.5 μl of DIO-ChR2-EYFP virus bilaterally. For all optogenetic experiments, we waited at least 3 weeks from viral injection to experimental stimulation to allow for sufficient ChR2 gene expression.

To confirm that DA neurons were transfected with ChR2 in animals used for optogenetic DA stimulation experiments, we perfused DAT-Cre mice that had been injected into the SNc with Cre-dependent ChR2-EYFP virus with 4% paraformaldehyde in PBS and post-fixed brains overnight. Coronal sections that included the injection site (SNc) and imaging site (dorsal striatum) were cut at 50 μM and immunolabeled using antibody against tyrosine hydroxylase [TH (1:1000); rabbit anti-TH, Millipore], the rate-limiting enzyme for catecholamine synthesis. Goat anti-rabbit DyLight 594 secondary antibody (1:1000; Invitrogen) was used to visualize TH. Image acquisition was performed on a Zeiss Axio ScanZ.1 using a 5× objective.

Image processing and data analysis of nIRCat fluorescence response

Raw movie files were processed using a custom-built MATLAB program (https://github.com/jtdbod/Nanosensor-Brain-Imaging). Briefly, for each raw movie stack (600 frames), a per-pixel $\Delta F/F$ defined as $(F - F_0)/F_0$ was calculated using the average intensity for the first 5% of frames as F_0, and F represents the dynamic fluorescence intensity at each pixel. ROIs were identified by calculating a median filter convolution and then performing thresholding using Otsu's method to identify ROIs with strong fluorescence modulation over background, followed by a morphological dilation operation. $\Delta F/F$ traces were then calculated for each generated ROI by averaging pixel values over the ROI. ROI sizes were computed using the measured pixel area and by approximating each as a circle to calculate an equivalent radius.

To compare responses across stimulation amplitudes and bath application of nomifensine, mean results were obtained as follows: First, all identified ROIs from a field of imaging were averaged. Mean traces were further averaged over different fields of view within the same slice and across slices (1 to 2 fields of view per slice and 1 to

2 slices per animal) and then averaged over experimental animals. Decay time constants (τ) were computed by fitting $\Delta F/F$ time traces to a first-order decay process on an ROI basis or field-of-view average basis. Latency to peak was computed as $t_{peak} - t_{stim}$, where t_{peak} is the time at which peak signal is attained and t_{stim} is time of stimulation. All statistical tests of significance (P values) were computed and reported from unpaired two-tailed t test.

ROI-level analysis of drug washes were computed by generating an ROI mask from one of the triplicate stimulations and then computing $\Delta F/F$ traces using the same ROI mask for all experimental runs (before and after application of drug). Each raw movie file was corrected for translational and rotational drift using StackReg plugin in FIJI and then processed using our custom MATLAB script. We removed all ROIs that were greater than 4 μm in size for subsequent analysis. For each ROI, post-to-pre drug ratios were computed as $(\Delta F/F)_{max\text{-}post\text{-}drug}/(\Delta F/F)_{max\text{-}pre\text{-}drug}$. Here, we define $(\Delta F/F)_{max}$ as the amplitude of nIRCat response in the post-stimulation epoch. Mean values from triplicate stimulation were used to evaluate the ratio.

SUPPLEMENTARY MATERIALS

Supplementary material for this article is available at http://advances.sciencemag.org/cgi/content/full/5/7/eaaw3108/DC1

Fig. S1. nIRCats are compatible with concentrations and conditions expected in brain tissue.
Fig. S2. Surface-immobilized single nIRCats are reversible upon repeat exposure to DA.
Fig. S3. Brain slice nIRCat loading protocol and schematic of visible and nIR fluorescence microscopy for imaging nIRCats in brain tissue.
Fig. S4. nIRCat imaging in *M. spicilegus* brain tissue.
Fig. S5. Intensity of nIRCat labeling at baseline does not predict site of Δ*F*/*F* hotspots.
Fig. S6. Variability in effect of quinpirole and sulpiride on nIRCat response on spatially segregated ROIs within a field of view.
Fig. S7. Data that confirm targeting of optogenetic stimulation of dopaminergic and glutamatergic inputs to the striatum.
Fig. S8. Effect of quinpirole on ChR2 evoked nIRCat response at the level of ROIs.
Fig. S9. Nomifensine extends nIRCat response to ChR2 stimulation of dopaminergic terminals in the dorsal striatum.
Movie S1. A representative movie from single-pulse electrical stimulation (0.3 mA) in dorsal striatum.
Movie S2. A representative movie from optogenetic stimulation (five pulses at 25 Hz, 1 mW mm^2) in dorsal striatum.

REFERENCES AND NOTES

1. B. A. Anderson, H. Kuwabara, D. F. Wong, E. G. Gean, A. Rahmim, J. R. Brašić, N. George, B. Frolov, S. M. Courtney, S. Yantis, The role of dopamine in value-based attentional orienting. *Curr. Biol.* **26**, 550–555 (2016).
2. M. V. Solanto, Dopamine dysfunction in AD/HD: integrating clinical and basic neuroscience research. *Behav. Brain Res.* **10**, 65–71 (2002).
3. J. Y. Cohen, S. Haesler, L. Vong, B. B. Lowell, N. Uchida, Neuron-type-specific signals for reward and punishment in the ventral tegmental area. *Nature* **482**, 88–88 (2012).
4. N. Eshel, J. Tian, M. Bukwich, N. Uchida, Dopamine neurons share common response function for reward prediction error. *Nat. Neurosci.* **19**, 479–486 (2016).
5. J. D. Berke, What does dopamine mean? *Nat. Neurosci.* **21**, 787–793 (2018).
6. E. E. Steinberg, R. Keiflin, J. R. Boivin, I. B. Witten, K. Deisseroth, P. H. Janak, A causal link between prediction errors, dopamine neurons and learning. *Nat. Neurosci.* **16**, 966–973 (2013).
7. A. A. Hamid, J. R. Pettibone, O. S. Mabrouk, V. L. Hetrick, R. Schmidt, C. M. Vander Weele, R. T. Kennedy, B. J. Aragona, J. D. Berke, Mesolimbic dopamine signals the value of work. *Nat. Neurosci.* **19**, 117–126 (2015).
8. J. D. Salamone, M. Correa, The mysterious motivational functions of mesolimbic dopamine. *Neuron* **76**, 470–485 (2012).
9. J. T. Dudman, J. W. Krakauer, The basal ganglia: From motor commands to the control of vigor. *Curr. Opin. Neurobiol.* **37**, 158–166 (2016).
10. J. Lotharius, P. Brundin, Pathogenesis of parkinson's disease: Dopamine, vesicles and α-synuclein. *Nat. Rev. Neurosci.* **3**, 932–942 (2002).
11. J. J. Weinstein, M. O. Chohan, M. Slifstein, L. S. Kegeles, H. Moore, A. Abi-Dargham, Pathway-specific dopamine abnormalities in schizophrenia. *Biol. Psychiatry* **81**, 31–42 (2017).
12. N. D. Volkow, J. S. Fowler, G.-J. Wang, J. M. Swanson, Dopamine in drug abuse and addiction: Results from imaging studies and treatment implications. *Mol. Psychiatry* **9**, 557–569 (2004).
13. J. D. Clements, R. A. Lester, G. Tong, C. E. Jahr, G. L. Westbrook, The time course of glutamate in the synaptic cleft. *Science* **258**, 1498–1501 (1992).
14. P. Greengard, The neurobiology of slow synaptic transmission. *Science* **294**, 1024–1030 (2001).
15. L. F. Agnati, M. Zoli, I. Strömberg, K. Fuxe, Intercellular communication in the brain: Wiring versus volume transmission. *Neuroscience* **69**, 711–726 (1995).
16. M. Zoli, C. Torri, R. Ferrari, A. Jansson, I. Zini, K. Fuxe, L. F. Agnati, The emergence of the volume transmission concept. *Brain Res. Rev.* **26**, 136–147 (1998).
17. M. E. Rice, S. J. Cragg, Dopamine spillover after quantal release: Rethinking dopamine transmission in the nigrostriatal pathway. *Brain Res. Rev.* **58**, 303–313 (2008).
18. S. J. Cragg, M. E. Rice, DAncing past the DAT at a DA synapse. *Trends Neurosci.* **27**, 270–277 (2004).
19. J. K. Dreyer, K. F. Herrik, R. W. Berg, J. D. Hounsgaard, Influence of phasic and tonic dopamine release on receptor activation. *J. Neurosci.* **30**, 14273–14283 (2010).
20. E. Marder, Neuromodulation of neuronal circuits: Back to the future. *Neuron* **76**, 1–11 (2012).
21. P. V. Jena, D. Roxbury, T. V. Galassi, L. Akkari, C. P. Horoszko, D. B. Iaea, J. Budhathoki-Uprety, N. Pipalia, A. S. Haka, J. D. Harvey, J. Mittal, F. R. Maxfield, J. A. Joyce, D. A. Heller, A carbon nanotube optical reporter maps endolysosomal lipid flux. *ACS Nano* **11**, 10689–10703 (2017).
22. P. W. Barone, S. Baik, D. A. Heller, M. S. Strano, Near-infrared optical sensors based on single-walled carbon nanotubes. *Nat. Mater.* **4**, 86–92 (2005).
23. J. D. Harvey, P. V. Jena, H. A. Baker, G. H. Zerze, R. M. Williams, T. V. Galassi, D. Roxbury, J. Mittal, D. A. Heller, A carbon nanotube reporter of microRNA hybridization events in vivo. *Nat. Biomed. Eng.* **1**, 0041 (2017).
24. A. G. Beyene, A. A. Alizadehmojarad, G. Dorlhiac, A. M. Streets, P. Král, L. Vuković, M. P. Landry, Ultralarge modulation of single wall carbon nanotube fluorescence mediated by neuromodulators adsorbed on arrays of oligonucleotide rings. *Nano. Lett.* **11**, 6995–7003 (2018).
25. G. Hong, S. Diao, J. Chang, A. L. Antaris, C. Chen, B. Zhang, S. Zhao, D. N. Atochin, P. L. Huang, K. I. Andreasson, C. J. Kuo, H. Dai, Through-skull fluorescence imaging of the brain in a new near-infrared window. *Nat. Photonics* **8**, 723–730 (2014).
26. J. Zhang, M. P. Landry, P. W. Barone, J.-H. Kim, S. Lin, Z. W. Ulissi, D. Lin, B. Mu, A. A. Boghossian, A. J. Hilmer, A. Rwei, A. C. Hinckley, S. Kruss, M. A. Shandell, N. Nair, S. Blake, F. Şen, S. Şen, R. G. Croy, D. Li, K. Yum, J.-H. Ahn, H. Jin, D. A. Heller, J. M. Essigmann, D. Blankschtein, M. S. Strano, Molecular recognition using corona phase complexes made of synthetic polymers adsorbed on carbon nanotubes. *Nat. Nanotechnol.* **8**, 959–968 (2013).
27. S. Kruss, M. P. Landry, E. Vander Ende, B. M. A. Lima, N. F. Reuel, J. Zhang, J. Nelson, B. Mu, A. Hilmer, M. Strano, Neurotransmitter detection using corona phase molecular recognition on fluorescent single-walled carbon nanotube sensors. *J. Am. Chem. Soc.* **136**, 713–724 (2014).
28. A. G. Beyene, I. R. McFarlane, R. L. Pinals, M. P. Landry, Stochastic simulation of dopamine neuromodulation for implementation of fluorescent neurochemical probes in the striatal extracellular space. *ACS Chem. Nerosci.* **8**, 2275–2289 (2017).
29. C. W. Berridge, B. D. Waterhouse, The locus coeruleus–noradrenergic system: Modulation of behavioral state and state-dependent cognitive processes. *Brain Res. Rev.* **42**, 33–84 (2003).
30. C. R. Gerfen, Synaptic organization of the striatum. *J. Electron Microsc. Tech.* **10**, 265–281 (1988).
31. N. X. Tritsch, B. L. Sabatini, Dopaminergic modulation of synaptic transmission in cortex and striatum. *Neuron* **76**, 33–50 (2012).
32. D. J. Piekarski, J. R. Boivin, L. Wilbrecht, Ovarian hormones organize the maturation of inhibitory neurotransmission in the frontal cortex at puberty onset in female mice. *Curr. Biol.* **27**, 1735–1745.e3 (2017).
33. A. G. Godin, J. A. Varela, Z. Gao, N. Danné, J. P. Dupuis, B. Lounis, L. Groc, L. Cognet, Single-nanotube tracking reveals the nanoscale organization of the extracellular space in the live brain. *Nat. Nanotechnol.* **12**, 238–243 (2017).
34. D. L. Robinson, B. J. Venton, M. L. A. V. Heien, R. M. Wightman, Detecting subsecond dopamine release with fast-scan cyclic voltammetry in vivo. *Clin. Chem.* **49**, 1763–1773 (2003).
35. M. L. A. V. Heien, M. A. Johnson, R. M. Wightman, Resolving neurotransmitters detected by fast-scan cyclic voltammetry. *Anal. Chem.* **76**, 5697–5704 (2004).
36. P. A. Garris, R. M. Wightman, Regional differences in dopamine release, uptake, and diffusion measured by fast-scan cyclic voltammetry. *Neuromethods Voltammetric Methods Brain Syst.* **27**, 179–220 (1995).
37. C. P. Ford, The role of D2-autoreceptors in regulating dopamine neuron activity and transmission. *Neuroscience* **282**, 13–22 (2014).
38. P. F. Marcott, S. Gong, P. Donthamsetti, S. G. Grinnell, M. N. Nelson, A. H. Newman, L. Birnbaumer, K. A. Martemyanov, J. A. Javitch, C. P. Ford, Regional heterogeneity of D2-receptor signaling in the dorsal striatum and nucleus accumbens. *Neuron* **98**, 575–587.e4 (2018).
39. A. Usiello, J.-H. Baik, F. Rougé-Pont, R. Picetti, A. Dierich, M. LeMeur, P. V. Piazza, E. Borrelli, Distinct functions of the two isoforms of dopamine D2 receptors. *Nature* **408**, 199–203 (2000).

40. F. Rougé-Pont, A. Usiello, M. Benoit-Marand, F. Gonon, P. V. Piazza, E. Borrelli, Changes in extracellular dopamine induced by morphine and cocaine: Crucial control by D2 receptors. *J. Neurosci.* **22**, 3293–3301 (2002).
41. F. Sun, J. Zeng, M. Jing, J. Zhou, J. Feng, S. F. Owen, Y. Luo, F. Li, H. Wang, T. Yamaguchi, Z. Yong, Y. Gao, W. Peng, L. Wang, S. Zhang, J. Du, D. Lin, M. Xu, A. C. Kreitzer, G. Cui, Y. Li, A genetically encoded fluorescent sensor enables rapid and specific detection of dopamine in flies, fish, and mice. *Cell* **174**, 481–496.e19 (2018).
42. T. Patriarchi, J. R. Cho, K. Merten, M. W. Howe, A. Marley, W.-H. Xiong, R. W. Folk, G. J. Broussard, R. Liang, M. J. Jang, H. Zhong, D. Dombeck, M. von Zastrow, A. Nimmerjahn, V. Gradinaru, J. T. Williams, L. Tian, Ultrafast neuronal imaging of dopamine dynamics with designed genetically encoded sensors. *Science* **360**, eaat4422 (2018).
43. D. B. Pereira, Y. Schmitz, J. Mészáros, P. Merchant, G. Hu, S. Li, A. Henke, J. E. Lizardi-Ortiz, R. J. Karpowicz Jr., T. J. Morgenstern, M. S. Sonders, E. Kanter, P. C. Rodriguez, E. V. Mosharov, D. Sames, D. Sulzer, Fluorescent false neurotransmitter reveals functionally silent dopamine vesicle clusters in the striatum. *Nat. Neurosci.* **19**, 578–586 (2016).
44. C. Liu, L. Kershberg, J. Wang, S. Schneeberger, P. S. Kaeser, Dopamine secretion is mediated by sparse active zone-like release sites. *Cell* **172**, 706–718.e15 (2018).
45. A. Mohebi, J. Pettibone, A. Hamid, J.-M. Wong, R. Kennedy, J. Berke, Forebrain dopamine value signals arise independently from midbrain dopamine cell firing. *Nature* **570**, 65–70 (2019).
46. D. A. Heller, E. S. Jeng, T.-K. Yeung, B. M. Martinez, A. E. Moll, J. B. Gastala, M. S. Strano, Optical detection of DNA conformational polymorphism on single-walled carbon nanotubes. *Science* **311**, 508–511 (2006).
47. L. Cognet, D. A. Tsyboulski, J.-D. R. Rocha, C. D. Doyle, J. M. Tour, R. B. Weisman, Stepwise quenching of exciton fluorescence in carbon nanotubes by single-molecule reactions. *Science* **316**, 1465–1468 (2007).
48. D. Roxbury, P. V. Jena, R. M. Williams, B. Enyedi, P. Niethammer, S. Marcet, M. Verhaegen, S. Blais-Ouellette, D. A. Heller, Hyperspectral microscopy of near-infrared fluorescence enables 17-chirality carbon nanotube imaging. *Sci. Rep.* **5**, 14167 (2015).
49. J. P. Giraldo, M. P. Landry, S.-Y. Kwak, R. M. Jain, M. H. Wong, N. M. Iverson, M. Ben-Naim, M. S. Strano, A ratiometric sensor using single chirality near-infrared fluorescent carbon nanotubes: Application to in vivo monitoring. *Small* **11**, 3973–3984 (2015).
50. J. T. D. Bonis-O'Donnell, R. H. Page, A. G. Beyene, E. G. Tindall, I. R. McFarlane, M. P. Landry, Dual near-infrared two-photon microscopy for deep-tissue dopamine nanosensor imaging. *Adv. Funct. Mater.* **27**, 1702112 (2017).
51. J. B. Ding, K. T. Takasaki, B. L. Sabatini, Supraresolution imaging in brain slices using stimulated-emission depletion two-photon laser scanning microscopy. *Neuron* **63**, 429–437 (2009).
52. F. Wang, G. Dukovic, L. E. Brus, T. F. Heinz, The optical resonances in carbon nanotubes arise from excitons. *Science* **308**, 838–841 (2005).
53. A. D. Edelstein, M. A. Tsuchida, N. Amodaj, H. Pinkard, R. D. Vale, N. Stuurman, Advanced methods of microscope control using μManager software. *J. Biol. Methods* **1**, 10 (2014).
54. A. Vandenberg, D. J. Piekarski, N. Caporale, F. J. Munoz-Cuevas, L. Wilbrecht, Adolescent maturation of inhibitory inputs onto cingulate cortex neurons is cell-type specific and TrkB dependent. *Front. Neural Circuits* **9**, 5 (2015).

Acknowledgments: We thank M. Feller, H. Bateup, D. Sulzer, and D. Schaffer for helpful discussions and comments on the manuscript and N. Ouassil for manuscript feedback. **Funding:** We acknowledge support of the NIH NIDA CEBRA Award no. R21DA044010 to L.W. and M.P.L. and the Burroughs Wellcome Fund Career Award at the Scientific Interface (CASI), the Simons Foundation, the Stanley Fahn PDF Junior Faculty Grant with award no. PF-JFA-1760, the Beckman Foundation Young Investigator Award, and the DARPA Young Investigator Award to M.P.L. M.P.L. is a Chan Zuckerberg Biohub investigator. A.G.B. was supported by the NSF Graduate Research Fellowship and an NIH DSPAN F99/K00 grant from NINDS and is an HHMI Gilliam Fellow. **Author contributions:** M.P.L. conceived the project with input from A.G.B. and L.W. A.G.B., K.D., M.P.L., and L.W. designed the studies and wrote the manuscript. A.G.B. performed most of the imaging experiments and the data analysis, and J.T.D.B.-O. automated the data analysis. K.D. performed whole-cell slice electrophysiological recordings. K.D., W.C.L., A.W.T., S.J.Y., D.J.P., and D.Y. performed the surgeries and assisted with the slice generation, control experiments, and nanosensor validation. P.K. performed the FSCV experiments. G.S.P. performed the *M. spicilegus* experiments. All authors edited and commented on the manuscript and gave their approval of the final version. **Competing interests:** M.L., L.W., J.T.D.B.-O., and A.G.B. are authors on a patent application pending with the Regents of the University of California (no. 16/373,542, published 12 April 2018). All other authors declare that they have no competing interests. **Data and materials availability:** All data needed to evaluate the conclusions in the paper are present in the paper and/or the Supplementary Materials. Additional data related to this paper may be requested from the authors. Custom processing software is available on GitHub (https://github.com/jtdbod/Nanosensor-Brain-Imaging).

Submitted 7 December 2018
Accepted 5 June 2019
Published 10 July 2019
10.1126/sciadv.aaw3108

Citation: A. G. Beyene, K. Delevich, J. T. Del Bonis-O'Donnell, D. J. Piekarski, W. C. Lin, A. W. Thomas, S. J. Yang, P. Kosillo, D. Yang, G. S. Prounis, L. Wilbrecht, M. P. Landry, Imaging striatal dopamine release using a nongenetically encoded near infrared fluorescent catecholamine nanosensor. *Sci. Adv.* **5**, eaaw3108 (2019).